




## Impact of strain-insensitive low-frequency phonon modes on lattice thermal transport in $A_2XB_6$ -type perovskites

Ruihuan Cheng <sup>1</sup>, Zezhu Zeng,<sup>1,2</sup> Chen Wang,<sup>1</sup> Niuchang Ouyang <sup>1</sup> and Yue Chen <sup>1,\*</sup>

<sup>1</sup>*Department of Mechanical Engineering, The University of Hong Kong, Pokfulam Road, Hong Kong SAR, China*

<sup>2</sup>*The Institute of Science and Technology Austria, Am Campus 1, 3400 Klosterneuburg, Austria*



(Received 14 November 2023; revised 11 January 2024; accepted 25 January 2024; published 14 February 2024)

Substrate induces mechanical strain on perovskite devices, which can result in alterations to its lattice dynamics and thermal transport. Herein, we have performed a theoretical investigation on the anharmonic lattice dynamics and thermal property of perovskite  $Rb_2SnBr_6$  and  $Cs_2SnBr_6$  under strains using perturbation theory up to the fourth-order terms and the unified thermal transport theory. We demonstrate a pronounced hardening of low-frequency optical phonons as temperature increases, indicating strong lattice anharmonicity and the necessity of adopting temperature-dependent interatomic force constants in the lattice thermal conductivity ( $\kappa_L$ ) calculations. It is found that the low-lying optical phonon modes of  $Rb_2SnBr_6$  are extremely soft and their phonon energies are almost strain independent, which ultimately lead to a lower  $\kappa_L$  and a weaker strain dependence than  $Cs_2SnBr_6$ . We further reveal that the strain dependence of these phonon modes in the  $A_2XB_6$ -type perovskites weakens as their vibrational frequency decreases. This study deepens the understanding of lattice thermal transport in perovskites  $A_2XB_6$  and provides a perspective on the selection of materials that meet the expected thermal behaviors in practical applications.

DOI: [10.1103/PhysRevB.109.054305](https://doi.org/10.1103/PhysRevB.109.054305)

### I. INTRODUCTION

Vacancy-ordered double perovskites  $A_2XB_6$  ( $A = K, Rb,$  and  $Cs$ ;  $X = Sn, Pb, Pt, Pd, Ti,$  and  $Te$ ;  $B = Cl, Br,$  and  $I$ ) have recently been demonstrated to be promising materials for photovoltaics, optoelectronics, and thermoelectrics due to their excellent optical, electrical, and thermophysical properties [1–11], as well as their stability in the ambient environment [12–14]. Despite extensive studies on their optical and electrical properties [1–11], the lattice thermal conductivity ( $\kappa_L$ ), which is essential for enhancing the performance of perovskite-based energy-conversion devices, has not been fully explored yet. Thermal conductivity plays a critical role in regulating the thermal management in devices, for example, its enhancement can efficiently dissipate heat in light-emitting diodes and solar cells, prolonging their operational lifetime [15–18]. On the other hand, efficient thermoelectric materials require a low thermal conductivity to maintain the temperature gradient [19–21]. In addition, perovskite coatings on the substrate can experience mechanical strain due to lattice mismatch [22–24]. Strain may also induce unexpected behaviors of thermal transport. Therefore, a microscopic investigation of the lattice dynamics and thermal transport of  $A_2XB_6$ -type perovskites is of great importance to optimize the thermal management in such energy conversion devices.

Recently, Sajjad *et al.* [9] reported first-principles calculations that the strong phonon scatterings induced by the mixing of low-lying optical modes with acoustic phonons in  $Cs_2PtI_6$  lead to an extremely low  $\kappa_L$  of  $0.15 \text{ Wm}^{-1}\text{K}^{-1}$

at 300 K. Ultralow  $\kappa_L$  obtained from computations are also reported in  $Cs_2SnBr_6$  [10,25] and  $Cs_2SnI_6$  [25] with  $0.12\sim 0.21 \text{ Wm}^{-1}\text{K}^{-1}$  and  $0.06 \text{ Wm}^{-1}\text{K}^{-1}$  at 300 K, respectively. A high-throughput screening study revealed that  $Rb_2SnBr_6$  has the lowest thermal conductivity at room temperature among the  $A_2XB_6$ -type perovskites [26]. Despite these investigations, anharmonic phonon frequency renormalization was ignored. Phonon frequency renormalization leads to alterations in the scattering phase space, which significantly influences phonon linewidths and ultimately exerts a crucial impact on  $\kappa_L$ . Similar effect has been observed in some perovskites (e.g.,  $Cs_2AgBiBr_6$  [27,28],  $Cs_2PbI_2Cl_2$  [29],  $BaZrO_3$  [30], and  $SrTiO_3$  [31]) and highly anharmonic solids (e.g.,  $UO_2$  [32],  $CeO_2$  [32],  $Cu_{12}Sb_4S_{13}$  [33],  $Ba_8Ga_{16}Ge_{30}$  [34], and  $YbFe_4Sb_{12}$  [35]). Pandey *et al.* [36] found that some optical phonons harden significantly with increasing temperature in  $Cs_2SnI_6$ , which reduces the scattering of heat-carrying acoustic phonons. Although pioneering studies have revealed lattice dynamics and thermal transport in some  $A_2XB_6$ -type perovskites, a comprehensive understanding of strain-induced alterations is urgently needed.

Here we investigate the temperature- and strain-dependent anharmonic lattice dynamics and thermal transport of perovskites  $Rb_2SnBr_6$  and  $Cs_2SnBr_6$  using perturbation theory up to the fourth-order anharmonicity, unified thermal transport theory [39], and molecular dynamics (MD) simulations with first-principles-based machine learning potentials. Our calculations reveal that the low-frequency optical phonon modes harden rapidly with increasing temperature, which is related to the vibrations of the Rb/Cs and Br atoms. By comparing the  $\kappa_L$  calculated from force constants (IFCs) extracted at different temperatures, we further reveal the effect

\*yuechen@hku.hk

of hardening of the low-lying optical modes on the thermal transport. The softer optical phonon modes of  $\text{Rb}_2\text{SnBr}_6$  lead to stronger phonon scatterings, which result in a lower  $\kappa_L$  than that of  $\text{Cs}_2\text{SnBr}_6$ . We also reveal weak strain-dependent optical modes in  $\text{Rb}_2\text{SnBr}_6$  along the  $\Gamma$ -X high-symmetry path at room temperature, which correspondingly lead to weaker strain-dependent  $\kappa_L$  compared to  $\text{Cs}_2\text{SnBr}_6$ . We further demonstrate that the strain dependence of the lowest-lying optical phonon frequency of  $\text{A}_2\text{XB}_6$ -type perovskites weakens for those with a lower frequency.

## II. METHODS

### A. Extraction of temperature-dependent force constants

We used the self-consistent harmonic Hamiltonian approximation method [38], as implemented in the Hiphive package [40], to compute the renormalized harmonic force constants at different temperatures and to extract the temperature-dependent second-order IFCs. A  $3 \times 3 \times 3$  supercell (243 atoms) was used to perform *ab initio* molecular dynamics (AIMD) simulations for 5 ps with a time step of 2 fs at different temperatures and then randomly extracted 50 configurations at each temperature. An energy cutoff value of 350 eV and a  $\Gamma$ -centering  $1 \times 1 \times 1$   $k$ -point mesh were used for AIMD simulations. The energies and interatomic forces of these configurations were then calculated from density functional theory (DFT) with an energy cutoff of 520 eV and a total energy convergence threshold of  $10^{-8}$  eV. The harmonic contributions at 0 K were subtracted from the force-displacement data prior to training the cluster space to accurately capture the anharmonic strength of third- and fourth-order IFCs [41]. Finally, the third- and fourth-order IFCs were extracted from these training data with second-, third-, and fourth-order neighbor cutoff distances of 8.5, 6.5 and 5.5 Å, respectively [Fig. S1].

### B. Construction of neuroevolution machine-learning potentials

To train a neuroevolution machine-learning potential (NEP) [42,43], we performed AIMD simulations with a  $3 \times 3 \times 3$  supercell (243 atoms) to generate randomly displaced configurations at different temperatures (100, 200, 300, 400, 500, 600, and 700 K) and configurations with uniform triaxial strains ranging from  $-3\%$  to  $3\%$ . We also incorporated 25 configurations with random small displacements to sample the low-temperature phase space of  $\text{Rb}_2\text{SnBr}_6$  and  $\text{Cs}_2\text{SnBr}_6$ . We totally obtained 675 configurations for each compound, among which 605 configurations were randomly selected for the training set and 70 configurations for the testing set. Accurate DFT calculations with a kinetic energy cutoff of 520 eV and a total energy tolerance of  $10^{-8}$  eV were performed to extract energies, forces, and stresses. The radial and angular cutoffs of the NEP were set at 8 and 5 Å, respectively, with a total of 200 000 generations applied to achieve convergence [Fig. S5]. The cross-validation results are shown in Fig. S6.

## III. RESULTS AND DISCUSSION

$\text{Rb}_2\text{SnBr}_6$  and  $\text{Cs}_2\text{SnBr}_6$  have a simple face-centered cubic lattice (space group  $Fm\bar{3}m$ ) with nine atoms in its

primitive cell, in which  $\text{Sn}^{4+}$  is bonded to six equivalent  $\text{Br}^-$  anions to form  $[\text{SnBr}_6]^{2-}$  octahedra that interact with the  $\text{Rb}^+/\text{Cs}^+$  cations, as shown in Figs. 1(a) and 1(b). We first study the anharmonic phonon frequency renormalizations of  $\text{Rb}_2\text{SnBr}_6$  and  $\text{Cs}_2\text{SnBr}_6$  using the self-consistent harmonic Hamiltonian approximation method [38]. Figures 1(c) and 1(d) show the calculated phonon dispersions of  $\text{Rb}_2\text{SnBr}_6$  and  $\text{Cs}_2\text{SnBr}_6$  from 0 to 700 K, respectively. It is seen that the high-frequency modes above 3 THz are rather insensitive to temperature for both two materials. In contrast, a significant hardening of the low-frequency optical modes ( $<3$  THz) is observed as temperature increases, implying that both compounds exhibit strong lattice anharmonicity. These phonon modes are dominated by the vibrations of Rb/Cs and Br atoms, as demonstrated by the atom-decomposed phonon density of states in Figs. 1(c) and 1(d). These atoms have loose bonding to the lattice, as evidenced by the relatively larger mean square displacements at 300 K for Rb/Cs and Br atoms comparing to the surrounding Sn atoms at 300 K [Fig. S3]. The prominent frequency renormalized mode at the  $\Gamma$  point corresponds to the dynamical rotation of  $[\text{SnBr}_6]^{2-}$  octahedra [11,36,44] [Figs. 1(e) and 1(f)], which exhibits a symmetric U-type local potential energy surface (PES) in  $\text{Cs}_2\text{SnBr}_6$ , and a double-well PES in  $\text{Rb}_2\text{SnBr}_6$ . The double-well PES explains the imaginary frequency of this mode in  $\text{Rb}_2\text{SnBr}_6$  at 0 K. The U-type PES of  $\text{Cs}_2\text{SnBr}_6$  is rather shallow, suggesting that the vibrational atoms associated with this phonon mode can easily deviate from the equilibrium positions [27,32].

We further investigate the effects of phonon frequency renormalization on the lattice thermal transports of  $\text{Rb}_2\text{SnBr}_6$  and  $\text{Cs}_2\text{SnBr}_6$  using the unified thermal transport theory developed by Simoncelli *et al.* [39], and the results are shown in Fig. 2(a) (see Supplemental Material (SM) for more computational details [45] [see also Refs. [33,35,36,39,46–64] therein]). It is noted that another unified thermal transport theory was developed by Isaeva *et al.* [65], which has been proven to be equivalent to the former [59,66]. The particlelike thermal conductivities ( $\kappa_L^p$ ) calculated using the second-order force constants at 300 K (IFCs-2nd-300 K) and the temperature-dependent second-order force constants (IFCs-2nd-TD) are strongly deviated, indicating that the renormalization of the phonon frequency has a significant effect on the  $\kappa_L^p$  of  $\text{Rb}_2\text{SnBr}_6$  and  $\text{Cs}_2\text{SnBr}_6$ . The temperature-induced phonon frequency renormalization of  $\text{Rb}_2\text{SnBr}_6$  is more pronounced than that of  $\text{Cs}_2\text{SnBr}_6$ . For instance, at  $\Gamma$  point, the frequency of the lowest-lying optical mode of  $\text{Rb}_2\text{SnBr}_6$  increases from 0.63 THz at 200 K to 0.90 THz at 600 K, while that of  $\text{Cs}_2\text{SnBr}_6$  rises from 1.10 to 1.29 THz. We also notice that the  $\kappa_L^p$  of  $\text{Rb}_2\text{SnBr}_6$  shows a weaker temperature dependence of  $\sim T^{-0.66}$  after considering the TD-IFCs.

The contribution of wavelike interband tunneling ( $\kappa_L^c$ ) to  $\kappa_L$  in strongly anharmonic materials cannot be ignored [33,36,39,51,57,58]. The calculated  $\kappa_L^c$  of both  $\text{Rb}_2\text{SnBr}_6$  and  $\text{Cs}_2\text{SnBr}_6$  show an increasing trend [Fig. 2(b)], which can be attributed to the broadened linewidths and the tight bunching of the low-frequency optical phonon modes [39,52]. By considering both particlelike propagation and wavelike tunneling contributions to thermal transport, the  $\kappa_L^{c+p}$  of  $\text{Rb}_2\text{SnBr}_6$  is found to be lower than that of  $\text{Cs}_2\text{SnBr}_6$  below 600 K as

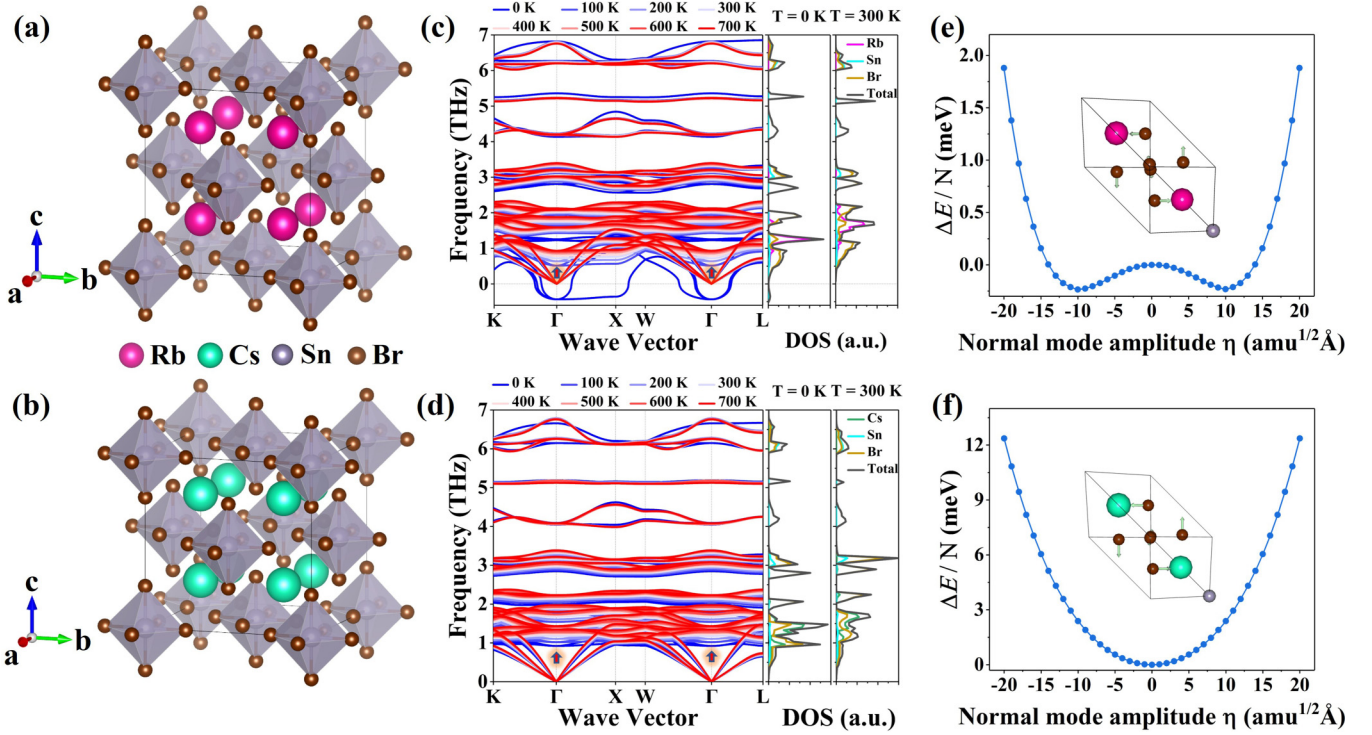


FIG. 1. Crystal structures of (a) Rb<sub>2</sub>SnBr<sub>6</sub> and (b) Cs<sub>2</sub>SnBr<sub>6</sub> visualized using VESTA [37]. Temperature-dependent phonon dispersions of (c) Rb<sub>2</sub>SnBr<sub>6</sub> and (d) Cs<sub>2</sub>SnBr<sub>6</sub> calculated using the self-consistent harmonic Hamiltonian approximation method [38] and the projected phonon density of states. The potential surfaces of the lowest-frequency phonon mode at  $\Gamma$  point and their visualized atomic rotations for (e) Rb<sub>2</sub>SnBr<sub>6</sub> and (f) Cs<sub>2</sub>SnBr<sub>6</sub>.

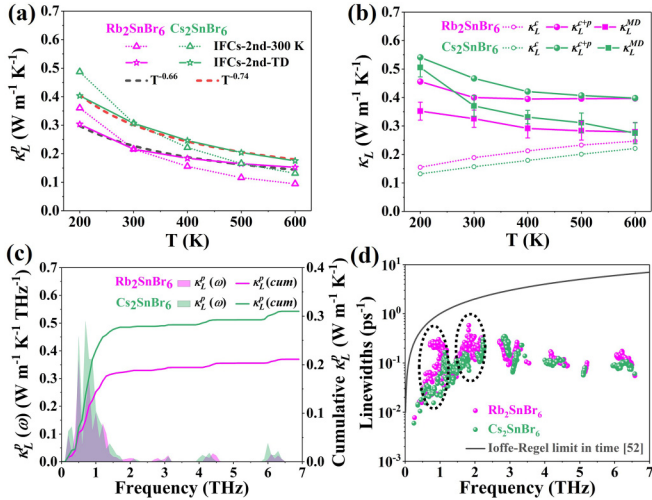


FIG. 2. (a) Lattice thermal conductivities contributed by the particlelike phonon propagation ( $\kappa_L^p$ ) of Rb<sub>2</sub>SnBr<sub>6</sub> and Cs<sub>2</sub>SnBr<sub>6</sub> calculated using two different sets of second-order interatomic force constants (IFCS-2nd; TD denotes temperature dependent). (b) Lattice thermal conductivities ( $\kappa_L^{c+p}$ ) of Rb<sub>2</sub>SnBr<sub>6</sub> and Cs<sub>2</sub>SnBr<sub>6</sub> calculated using temperature-dependent IFCS-2nd based on the unified theory [39]. The HNEMD results ( $\kappa_L^{MD}$ ) are also shown for comparison. (c) Comparisons of particle-like phonon propagation spectra ( $\kappa_L^p(\omega)$ ) and the cumulative values between Rb<sub>2</sub>SnBr<sub>6</sub> and Cs<sub>2</sub>SnBr<sub>6</sub> at 300 K. (d) Comparison of frequency-dependent phonon linewidths between Rb<sub>2</sub>SnBr<sub>6</sub> and Cs<sub>2</sub>SnBr<sub>6</sub> at 300 K.

shown in Fig. 2(b), despite that Cs<sub>2</sub>SnBr<sub>6</sub> contains heavier element Cs. This finding is consistent with the results obtained from homogeneous nonequilibrium molecular dynamics (HNEMD) simulations ( $\kappa_L^{MD}$ ) [61,62,67] (see SM for more details [45]) based on a neuroevolution machine-learning potential [43] [Fig. 2(b)], as implemented in the GPUMD package [63]. The difference in thermal conductivity calculated from MD simulations and unified thermal transport theory may be related to the lattice anharmonicity above the fourth order [51,68,69] and the large atomic vibration.

As the  $\kappa_L^c$  of Rb<sub>2</sub>SnBr<sub>6</sub> is higher than that of Cs<sub>2</sub>SnBr<sub>6</sub>, the lower  $\kappa_L^{c+p}$  of Rb<sub>2</sub>SnBr<sub>6</sub> is due to its lower particle-like propagation term  $\kappa_L^p$ . It is seen from Fig. 2(c) that the lower  $\kappa_L^p$  term of Rb<sub>2</sub>SnBr<sub>6</sub> at 300 K is mainly due to the suppression of phonon propagation in the frequency range of 0.5~1.0 THz. In this range, the low-frequency optical phonon modes in Rb<sub>2</sub>SnBr<sub>6</sub> exhibit strong couplings with the acoustic phonon modes. The enhanced phonon scatterings lead to suppressed phonon thermal transport of Rb<sub>2</sub>SnBr<sub>6</sub>, as evidenced by its significantly larger linewidths compared to Cs<sub>2</sub>SnBr<sub>6</sub> [Fig. 2(d)]. It is noted that the phonons are well-defined with linewidths smaller than their corresponding frequencies [Fig. 2(d)]. Therefore, the unified thermal transport theory adopted in this work is reliable for calculating  $\kappa_L$  [52,59]. In the case where overdamped phonons dominate, the full phonon spectral density approach in Wigner's [59] or Hardy's [70] heat flux space is needed for more rigorous evaluation.



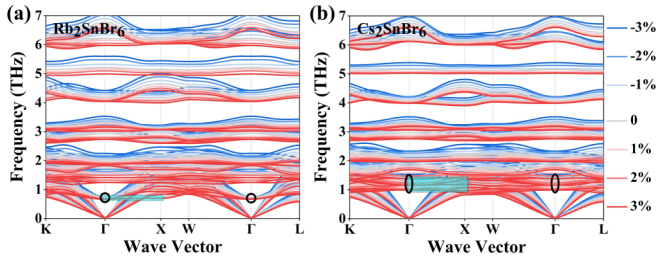


FIG. 3. Phonon dispersions of (a)  $\text{Rb}_2\text{SnBr}_6$  and (b)  $\text{Cs}_2\text{SnBr}_6$  at 300 K calculated using the self-consistent harmonic Hamiltonian approximation method under uniform triaxial strains from  $-3\%$  to  $+3\%$ . The highlighted phonon modes respond differently to strain.

Pervious studies [71–74] also indicate that strain engineering is an effective method to manipulate the low-lying phonon modes and thus affect the thermal transport of strongly anharmonic materials. By introducing uniform triaxial strain, we reveal that the phonon dispersions of  $\text{Cs}_2\text{SnBr}_6$  exhibit a strong dependence on strain at 300 K. Phonons are found to soften under tensile strain and harden under compressive strain. Most of the phonon modes of  $\text{Rb}_2\text{SnBr}_6$  also exhibit strong strain dependence, while the relatively nondispersive low-lying optical modes between  $\Gamma$  and X, as highlighted in Fig. 3(a) by the blue frame, show weak strain dependence. The distinct responses of the phonon modes to strain inevitably result in different lattice thermal transport properties between  $\text{Rb}_2\text{SnBr}_6$  and  $\text{Cs}_2\text{SnBr}_6$  under strains, as shown in Fig. 4. At room temperature, the  $\kappa_L^c$  of  $\text{Rb}_2\text{SnBr}_6$  and  $\text{Cs}_2\text{SnBr}_6$  are almost unaffected by strain, while the  $\kappa_L^p$  are more sensitive to strain [Fig. 4(a)]. Additionally, the strain dependences of  $\kappa_L^p$  and  $\kappa_L^{c+p}$  of  $\text{Rb}_2\text{SnBr}_6$  are considerably weaker than those of  $\text{Cs}_2\text{SnBr}_6$ , e.g.,  $\kappa_L^p$  and  $\kappa_L^{c+p}$  of  $\text{Rb}_2\text{SnBr}_6$  and  $\text{Cs}_2\text{SnBr}_6$  at  $+3\%$  strain are similar, but they become very different at  $-3\%$  strain, although the phonon group velocities under strains are similar [Fig. S8].

From the spectral particlelike thermal conductivity ( $\kappa_L^p(\omega)$ ) [Fig. 4(b)], we find that the different strain dependences of  $\text{Rb}_2\text{SnBr}_6$  and  $\text{Cs}_2\text{SnBr}_6$  arise from the phonon modes in the frequency range of  $0.5\sim 1.0$  THz. Within this range, the lowest-lying optical phonon modes of  $\text{Rb}_2\text{SnBr}_6$  along the  $\Gamma$ -X path, whose frequencies are insensitive to strain, maintain strong scatterings with the acoustic phonon modes, leading to a weaker strain dependence of the particlelike

thermal transport. On the contrary, the frequency of the lowest-lying optical modes of  $\text{Cs}_2\text{SnBr}_6$  are more sensitive to strain, leading to its phonon thermal transport being more easily altered under strains.

$\text{Rb}_2\text{SnBr}_6$  and  $\text{Cs}_2\text{SnBr}_6$  have similar  $\kappa_L^p$  at  $+3\%$  (tensile) strain. It is seen from Fig. 4(c) that  $\text{Rb}_2\text{SnBr}_6$  and  $\text{Cs}_2\text{SnBr}_6$  also display comparable phonon linewidths at  $+3\%$  strain. As compressive (negative) strain is applied,  $\text{Rb}_2\text{SnBr}_6$  maintains strong phonon scatterings as evidenced by the large phonon linewidths at  $-3\%$  strain. On the contrary, the phonon scatterings in  $\text{Cs}_2\text{SnBr}_6$  are strongly suppressed, as demonstrated by the reduced phonon linewidths at  $-3\%$  strain. The strain dependence of phonon linewidths in  $\text{Rb}_2\text{SnBr}_6$  is relatively weak compared to  $\text{Cs}_2\text{SnBr}_6$ . Thus, the disparity in linewidths between  $\text{Rb}_2\text{SnBr}_6$  and  $\text{Cs}_2\text{SnBr}_6$  amplifies with increasing compressive strain, leading to a more pronounced impact of strain on the  $\kappa_L^p$  of  $\text{Cs}_2\text{SnBr}_6$  than that of  $\text{Rb}_2\text{SnBr}_6$ .

We further extend the study of the strain dependences of the lowest-lying optical modes at  $\Gamma$  and X points to other  $\text{A}_2\text{XB}_6$ -type perovskites, as shown in Fig. 5 (see Fig. S9 for the phonon dispersions). It is found that in these perovskites, the frequency of the phonon modes decreases with increasing uniform triaxial tensile strain and increases with increasing compressive strain. This strain dependence weakens with the decrease of the phonon frequency, for example, the frequencies of the lowest-lying optical modes of  $\text{Rb}_2\text{SnBr}_6$  and  $\text{Cs}_2\text{SnI}_6$  are lower than those of  $\text{Cs}_2\text{SnCl}_6$  and  $\text{Rb}_2\text{SnCl}_6$ , and their strain dependences are significantly weaker than those of  $\text{Cs}_2\text{SnCl}_6$  and  $\text{Rb}_2\text{SnCl}_6$ . This is related to the rotational vibration of the lowest-lying optical mode, and a lower frequency corresponds to a weaker interaction with the surrounding chemical environment. To provide further insight, we have calculated the electron density distributions [Figs. S10(a) and S10(b)]. We find a stronger overlapping charge cloud between the Sn and Cl atoms within the  $[\text{SnCl}_6]^{2-}$  octahedra than that between the Sn and Br atoms within the  $[\text{SnBr}_6]^{2-}$  octahedra, suggesting that Sn-Cl has a stronger bonding than Sn-Br, which is also consistent with the steeper potential energy surface of Cl atom comparing to that of the Br atom [Fig. S10(c)]. Based on the above discussion,  $\text{A}_2\text{XB}_6$ -type perovskites with weak strain-dependent low-lying phonon modes may also show weaker strain-dependent  $\kappa_L$ , suggesting smaller thermal conductivity alteration in the presence of strain.

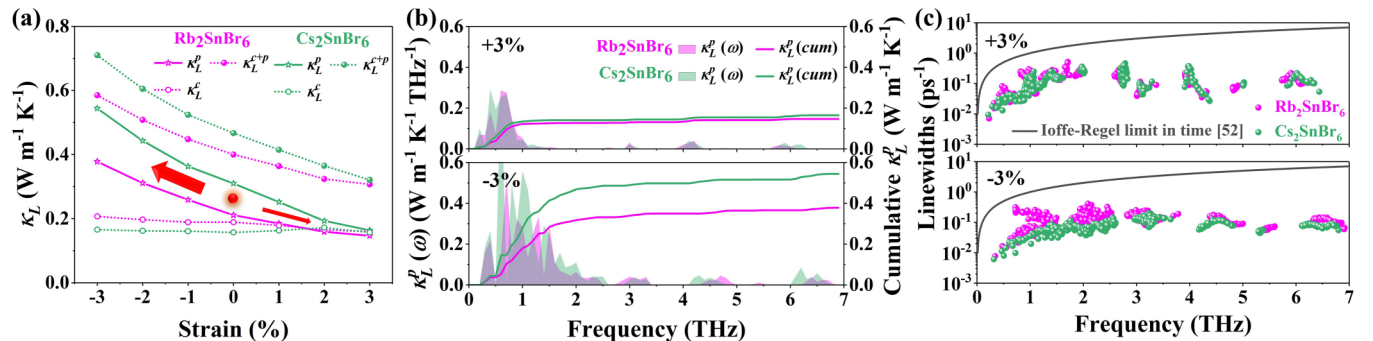


FIG. 4. (a) Lattice thermal conductivities of  $\text{Rb}_2\text{SnBr}_6$  and  $\text{Cs}_2\text{SnBr}_6$  at 300 K under uniform triaxial strains. Comparisons of frequency-dependent (b)  $\kappa_L^p(\omega)$  and (c) phonon linewidths between  $\text{Rb}_2\text{SnBr}_6$  and  $\text{Cs}_2\text{SnBr}_6$  at 300 K.

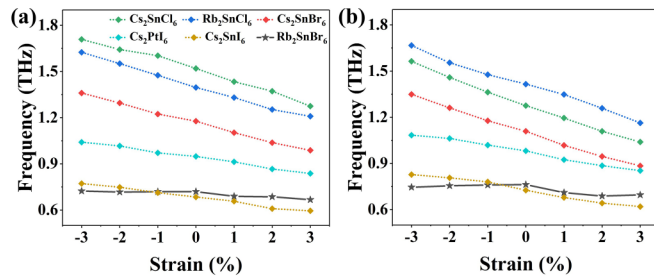


FIG. 5. The strain-dependent phonon frequencies of the lowest-lying optical phonon modes at (a)  $\Gamma$  and (b) X points for six  $A_2XB_6$ -type double perovskites at 300 K.

#### IV. CONCLUSION

In conclusion, the anharmonic lattice dynamics and thermal transport of perovskites  $Rb_2SnBr_6$  and  $Cs_2SnBr_6$  at

elevated temperatures and under strains are investigated. Our results show that phonon frequency renormalization is critical for calculating the lattice thermal conductivity. We find that the low-frequency optical modes have a significant effect on the lattice thermal transport, as they have pronounced scatterings with the acoustic phonon modes. We also reveal that if the zone center and X-point lowest-lying optical phonon modes of  $A_2XB_6$ -type perovskites have lower frequencies, they have weaker strain dependences and thus the lattice thermal conductivity will be less affected by strain.

#### ACKNOWLEDGMENTS

This work is supported by the Research Grants Council of Hong Kong (C7002-22Y and 17318122). The authors are grateful for the research computing facilities offered by ITS, HKU. Z.Z. acknowledges the European Union's Horizon 2020 research and innovation programme under the Marie Skłodowska-Curie Grant Agreement No. 101034413.

- [1] P. Zhou, H. Chen, Y. Chao, Q. Zhang, W. Zhang, F. Lv, L. Gu, Q. Zhao, N. Wang, J. Wang *et al.*, Single-atom Pt-I<sub>3</sub> sites on all-inorganic  $Cs_2SnI_6$  perovskite for efficient photocatalytic hydrogen production, *Nat. Commun.* **12**, 4412 (2021).
- [2] B. Lee, C. C. Stoumpos, N. Zhou, F. Hao, C. Malliakas, C.-Y. Yeh, T. J. Marks, M. G. Kanatzidis, and R. P. H. Chang, Air-stable molecular semiconducting iodosalts for solar cell applications:  $Cs_2SnI_6$  as a hole conductor, *J. Am. Chem. Soc.* **136**, 15379 (2014).
- [3] S. Yang, L. Wang, S. Zhao, A. Liu, Y. Zhou, Q. Han, F. Yu, L. Gao, C. Zhang, and T. Ma, Novel lead-free material  $Cs_2PtI_6$  with narrow bandgap and ultra-stability for its photovoltaic application, *ACS Appl. Mater. Interfaces* **12**, 44700 (2020).
- [4] D. S. Dolzhenkov, C. Wang, Y. Xu, M. G. Kanatzidis, and E. A. Weiss, Ligand-free, quantum-confined  $Cs_2SnI_6$  perovskite nanocrystals, *Chem. Mater.* **29**, 7901 (2017).
- [5] M. Hussain, M. Rashid, A. Ali, M. F. Bhopal, and A. Bhatti, Systematic study of optoelectronic and transport properties of cesium lead halide ( $Cs_2PbX_6$ ;  $X = Cl, Br, I$ ) double perovskites for solar cell applications, *Ceram. Inte.* **46**, 21378 (2020).
- [6] M. Faizan, K. C. Bhamu, G. Murtaza *et al.* Electronic and optical properties of vacancy ordered double perovskites  $A_2BX_6$  ( $A=Rb, Cs$ ;  $B=Sn, Pd, Pt$ ; and  $X=Cl, Br, I$ ) a first principles study, *Sci. Rep.* **11**, 6965 (2021).
- [7] P. D. Sreedevi and P. Ravindran, Revealing the optoelectronic properties of tin-based vacancy ordered double perovskites:  $K_2SnBr_6$  and  $Rb_2SnBr_6$ , *AIP Conf. Proc.* **2369**, 020149 (2021).
- [8] D.-Y. Hu, X.-H. Zhao, T.-Y. Tang, L.-M. Lu, L. Li, L.-K. Gao, and Y.-L. Tang, First-principles calculations to investigate the structural, electronic and optical properties of lead-free double perovskites  $Rb_2SeI_6$  and  $K_2SeI_6$ , *Sol. Energy* **231**, 236 (2022).
- [9] M. Sajjad, Q. Mahmood, N. Singh, and J. A. Larsson, Ultralow lattice thermal conductivity in double perovskite  $Cs_2PtI_6$ : A promising thermoelectric material, *ACS Appl. Energy Mater.* **3**, 11293 (2020).
- [10] X. Zeng, J. Jiang, G. Niu, L. Sui, Y. Zhang, X. Wang, X. Liu, A. Chen, M. Jin, and K. Yuan, Physical insights on the thermoelectric performance of  $Cs_2SnBr_6$  with ultralow lattice thermal conductivity, *J. Phys. Chem. Lett.* **13**, 9736 (2022).
- [11] A. Bhui, T. Ghosh, K. Pal, K. Singh Rana, K. Kundu, A. Soni, and K. Biswas, Intrinsically low thermal conductivity in the n-type vacancy-ordered double perovskite  $Cs_2SnI_6$ : Octahedral rotation and anharmonic rattling, *Chem. Mater.* **34**, 3301 (2022).
- [12] M. Hamdan and A. K. Chandiran,  $Cs_2PtI_6$  halide perovskite is stable to air, moisture, and extreme pH: application to photoelectrochemical solar water oxidation, *Angew. Chem.* **132**, 16167 (2020).
- [13] Y. Cai, W. Xie, H. Ding, Y. Chen, K. Thirumal, L. H. Wong, N. Mathews, S. G. Mhaisalkar, M. Sherburne, and M. Asta, Computational study of halide perovskite-derived  $A_2XB_6$  inorganic compounds: Chemical trends in electronic structure and structural stability, *Chem. Mater.* **29**, 7740 (2017).
- [14] N. R. Wolf, B. A. Connor, A. H. Slavney, and H. I. Karunadasa, Doubling the stakes: The promise of halide double perovskites, *Angew. Chem.* **133**, 16400 (2021).
- [15] G. Li, K. Chen, Y. Cui, Y. Zhang, Y. Tian, B. Tian, Y. Hao, Y. Wu, and H. Zhang, Stability of perovskite light sources: Status and challenges, *Adv. Opt. Mater.* **8**, 1902012 (2020).
- [16] L. Zhang, Y. Xie, Z. Tian, Y. Liu, C. Geng, and S. Xu, Thermal conductive encapsulation enables stable high-power perovskite-converted light-emitting diodes, *ACS Appl. Mater. Interfaces* **13**, 30076 (2021).
- [17] K. Choi, J. Lee, H. Choi, G.-W. Kim, H. I. Kim, and T. Park, Heat dissipation effects on the stability of planar perovskite solar cells, *Energy Environ. Sci.* **13**, 5059 (2020).
- [18] N. Yang, F. Pei, J. Dou, Y. Zhao, Z. Huang, Y. Ma, S. Ma, C. Wang, X. Zhang, H. Wang, C. Zhu, Y. Bai, H. Zhou, T. Song, Y. Chen, and Q. Chen, Improving heat transfer enables durable perovskite solar cells, *Adv. Energy Mater.* **12**, 2200869 (2022).
- [19] J. He and T. M. Tritt, Advances in thermoelectric materials research: Looking back and moving forward, *Science* **357**, eaak9997 (2017).

- [20] H. Xie, S. Hao, J. Bao, T. J. Slade, G. J. Snyder, C. Wolverton, and M. G. Kanatzidis, All-inorganic halide perovskites as potential thermoelectric materials: Dynamic cation off-centering induces ultralow thermal conductivity, *J. Am. Chem. Soc.* **142**, 9553 (2020).
- [21] M. A. Haque, S. Kee, D. R. Villalva, W.-L. Ong, and D. Baran, Halide perovskites: Thermal transport and prospects for thermoelectricity, *Adv. Sci.* **7**, 1903389 (2020).
- [22] J. Zhao, Y. Deng, H. Wei, X. Zheng, Z. Yu, Y. Shao, J. E. Shield, and J. Huang, Strained hybrid perovskite thin films and their impact on the intrinsic stability of perovskite solar cells, *Sci. Adv.* **3**, eaao5616 (2017).
- [23] C. Zhu, X. Niu, Y. Fu, N. Li, C. Hu, Y. Chen, X. He, G. Na, P. Liu, H. Zai *et al.*, Strain engineering in perovskite solar cells and its impacts on carrier dynamics, *Nat. Commun.* **10**, 815 (2019).
- [24] D. Liu, D. Luo, A. N. Iqbal, K. W. Orr, T. A. Doherty, Z.-H. Lu, S. D. Stranks, and W. Zhang, Strain analysis and engineering in halide perovskite photovoltaics, *Nat. Mater.* **20**, 1337 (2021).
- [25] M. Fallah and H. Milani Moghaddam, Ultra-low lattice thermal conductivity and high thermoelectric efficiency in  $\text{Cs}_2\text{SnX}_6$  ( $X = \text{Br}, \text{I}$ ): A DFT study, *Mater. Sci. Semicond. Process* **133**, 105984 (2021).
- [26] J. Li, W. Hu, and J. Yang, High-throughput screening of rattling-induced ultralow lattice thermal conductivity in semiconductors, *J. Am. Chem. Soc.* **144**, 4448 (2022).
- [27] J. Klarbring, O. Hellman, I. A. Abrikosov, and S. I. Simak, Anharmonicity and ultralow thermal conductivity in lead-free halide double perovskites, *Phys. Rev. Lett.* **125**, 045701 (2020).
- [28] C. Lin, G. Hautier, R. Guo, and B. Huang, Unravelling ultralow thermal conductivity in perovskite  $\text{Cs}_2\text{AgBiBr}_6$ : dominant wave-like phonon tunnelling and strong anharmonicity, *npj Comput. Mater.* **10**, 30 (2024).
- [29] Z. Zeng, C. Chen, C. Zhang, Q. Zhang, and Y. Chen, Critical phonon frequency renormalization and dual phonon coexistence in layered Ruddlesden-Popper inorganic perovskites, *Phys. Rev. B* **105**, 184303 (2022).
- [30] J. Zheng, D. Shi, Y. Yang, C. Lin, H. Huang, R. Guo, and B. Huang, Anharmonicity-induced phonon hardening and phonon transport enhancement in crystalline perovskite  $\text{BaZrO}_3$ , *Phys. Rev. B* **105**, 224303 (2022).
- [31] Q. Wang, Z. Zeng, and Y. Chen, Revisiting phonon transport in perovskite  $\text{SrTiO}_3$ : Anharmonic phonon renormalization and four-phonon scattering, *Phys. Rev. B* **104**, 235205 (2021).
- [32] S.-Y. Yue, X. Zhang, G. Qin, S. R. Phillpot, and M. Hu, Metric for strong intrinsic fourth-order phonon anharmonicity, *Phys. Rev. B* **95**, 195203 (2017).
- [33] Y. Xia, V. Ozoliņš, and C. Wolverton, Microscopic mechanisms of glasslike lattice thermal transport in cubic  $\text{Cu}_{12}\text{Sb}_4\text{S}_{13}$  tetrahedrites, *Phys. Rev. Lett.* **125**, 085901 (2020).
- [34] T. Tadano and S. Tsuneyuki, Quartic anharmonicity of rattlers and its effect on lattice thermal conductivity of clathrates from first principles, *Phys. Rev. Lett.* **120**, 105901 (2018).
- [35] J. Zheng, D. Shi, S. Liu, Y. Yang, C. Lin, Z. Chang, R. Guo, and B. Huang, Effects of high-order anharmonicity on anomalous lattice dynamics and thermal transport in fully filled skutterudite  $\text{YbFe}_4\text{Sb}_{12}$ , *Phys. Rev. Mater.* **6**, 093801 (2022).
- [36] T. Pandey, M.-H. Du, D. S. Parker, and L. Lindsay, Origin of ultralow phonon transport and strong anharmonicity in lead-free halide perovskites, *Mater. Today Phys.* **28**, 100881 (2022).
- [37] K. Momma and F. Izumi, VESTA: A three-dimensional visualization system for electronic and structural analysis, *J. Appl. Crystallogr.* **41**, 653 (2008).
- [38] I. Errea, M. Calandra, and F. Mauri, Anharmonic free energies and phonon dispersions from the stochastic self-consistent harmonic approximation: Application to platinum and palladium hydrides, *Phys. Rev. B* **89**, 064302 (2014).
- [39] M. Simoncelli, N. Marzari, and F. Mauri, Unified theory of thermal transport in crystals and glasses, *Nat. Phys.* **15**, 809 (2019).
- [40] F. Eriksson, E. Fransson, and P. Erhart, The Hiphive package for the extraction of high-order force constants by machine learning, *Adv. Theory Simul.* **2**, 1800184 (2019).
- [41] Y. Xia, V. I. Hegde, K. Pal, X. Hua, D. Gaines, S. Patel, J. He, M. Aykol, and C. Wolverton, High-throughput study of lattice thermal conductivity in binary rocksalt and zinc blende compounds including higher-order anharmonicity, *Phys. Rev. X* **10**, 041029 (2020).
- [42] Z. Fan, Z. Zeng, C. Zhang, Y. Wang, K. Song, H. Dong, Y. Chen, and T. Ala-Nissila, Neuroevolution machine learning potentials: Combining high accuracy and low cost in atomistic simulations and application to heat transport, *Phys. Rev. B* **104**, 104309 (2021).
- [43] Z. Fan, Improving the accuracy of the neuroevolution machine learning potential for multi-component systems, *J. Phys.: Condens. Matter* **34**, 125902 (2022).
- [44] A. E. Maughan, A. M. Ganose, M. A. Almaker, D. O. Scanlon, and J. R. Neilson, Tolerance factor and cooperative tilting effects in vacancy-ordered double perovskite halides, *Chem. Mater.* **30**, 3909 (2018).
- [45] See Supplemental Material at <http://link.aps.org/supplemental/10.1103/PhysRevB.109.054305> for further details on density functional theory calculations, lattice thermal conductivity computed from the unified thermal transport theory, mean squared displacement, construction of neuroevolution machine-learning potentials, homogeneous nonequilibrium molecular dynamics, phonon properties of perovskites under strains.
- [46] G. Kresse and J. Furthmüller, Efficient iterative schemes for *ab initio* total-energy calculations using a plane-wave basis set, *Phys. Rev. B* **54**, 11169 (1996).
- [47] G. Kresse and D. Joubert, From ultrasoft pseudopotentials to the projector augmented-wave method, *Phys. Rev. B* **59**, 1758 (1999).
- [48] J. P. Perdew, A. Ruzsinszky, G. I. Csonka, O. A. Vydrov, G. E. Scuseria, L. A. Constantin, X. Zhou, and K. Burke, Restoring the density-gradient expansion for exchange in solids and surfaces, *Phys. Rev. Lett.* **100**, 136406 (2008).
- [49] W. Li, J. Carrete, N. A. Katcho, and N. Mingo, ShengBTE: A solver of the Boltzmann transport equation for phonons, *Comput. Phys. Commun.* **185**, 1747 (2014).
- [50] T. Feng and X. Ruan, Quantum mechanical prediction of four-phonon scattering rates and reduced thermal conductivity of solids, *Phys. Rev. B* **93**, 045202 (2016).
- [51] Z. Zeng, C. Zhang, Y. Xia, Z. Fan, C. Wolverton, and Y. Chen, Nonperturbative phonon scatterings and the two-channel thermal transport in  $\text{Ti}_3\text{VSe}_4$ , *Phys. Rev. B* **103**, 224307 (2021).
- [52] M. Simoncelli, N. Marzari, and F. Mauri, Wigner formulation of thermal transport in solids, *Phys. Rev. X* **12**, 041011 (2022).

- [53] G. Markstein and H. Nowotny, Die kristallstruktur von bromstannaten  $A_2SnBr_6$  ( $A = Cs, Rb, NH_4, K$ ), *Z. Kristall.-Crystall. Mater.* **100**, 265 (1939).
- [54] A. Kaltzoglou, M. Antoniadou, A. G. Kontos, C. C. Stoumpos, D. Perganti, E. Siranidi, V. Raptis, K. Trohidou, V. Psycharis, M. G. Kanatzidis *et al.*, Optical-vibrational properties of the  $Cs_2SnX_6$  ( $X = Cl, Br, I$ ) defect perovskites and hole-transport efficiency in dye-sensitized solar cells, *J. Phys. Chem. C* **120**, 11777 (2016).
- [55] S. A. Qamar, T.-W. Lin, Y.-T. Tsai, and C. C. Lin, Lead-free  $Rb_2SnCl_6$ : Bi perovskite nanocrystals for luminescence emission, *ACS Appl. Nano Mater.* **5**, 7580 (2022).
- [56] G. Thiele, C. Mrozek, D. Kämmerer, and K. Wittmann, Über hexaiodoplatinate(IV)  $M_2PtI_6$  ( $M = K, Rb, Cs, NH_4, Tl$ ) darstellungsverfahren, eigenschaften und kristallstrukturen/on hexaiodoplatinates(IV)  $M_2PtI_6$  ( $M = K, Rb, Cs, NH_4, Tl$ ) - preparation, properties and structural data, *Z. Naturforsch. B* **38**, 905 (1983).
- [57] Z. Zhang, Y. Guo, M. Bescond, J. Chen, M. Nomura, and S. Volz, Heat conduction theory including phonon coherence, *Phys. Rev. Lett.* **128**, 015901 (2022).
- [58] X. Wang, Z. Gao, G. Zhu, J. Ren, L. Hu, J. Sun, X. Ding, Y. Xia, and B. Li, Role of high-order anharmonicity and off-diagonal terms in thermal conductivity: A case study of multiphase  $CsPbBr_3$ , *Phys. Rev. B* **107**, 214308 (2023).
- [59] G. Caldarelli, M. Simoncelli, N. Marzari, F. Mauri, and L. Benfatto, Many-body Green's function approach to lattice thermal transport, *Phys. Rev. B* **106**, 024312 (2022).
- [60] W. Lai, Y. Wang, D. T. Morelli, and X. Lu, From bonding asymmetry to anharmonic rattling in  $Cu_{12}Sb_4S_{13}$  tetrahedrites: When lone-pair electrons are not so lonely, *Adv. Funct. Mater.* **25**, 3648.
- [61] Z. Fan, H. Dong, A. Harju, and T. Ala-Nissila, Homogeneous nonequilibrium molecular dynamics method for heat transport and spectral decomposition with many-body potentials, *Phys. Rev. B* **99**, 064308 (2019).
- [62] D. J. Evans, Homogeneous nemd algorithm for thermal conductivity-application of non-canonical linear response theory, *Phys. Lett. A* **91**, 457 (1982).
- [63] Z. Fan, Y. Wang, P. Ying, K. Song, J. Wang, Y. Wang, Z. Zeng, K. Xu, E. Lindgren, J. M. Rahm, A. J. Gabourie, J. Liu, H. Dong, J. Wu, Y. Chen, Z. Zhong, J. Sun, P. Erhart, Y. Su, and T. Ala-Nissila, GPUMD: A package for constructing accurate machine-learned potentials and performing highly efficient atomistic simulations, *J. Chem. Phys.* **157**, 114801 (2022).
- [64] M. Tuckerman, *Statistical Mechanics: Theory and Molecular Simulation*, Oxford Graduate Texts (Oxford University Press, Oxford, 2010).
- [65] L. Isaeva, G. Barbalinardo, D. Donadio, and S. Baroni, Modeling heat transport in crystals and glasses from a unified lattice-dynamical approach, *Nat. Commun.* **10**, 3853 (2019).
- [66] A. Fiorentino and S. Baroni, From Green-Kubo to the full Boltzmann kinetic approach to heat transport in crystals and glasses, *Phys. Rev. B* **107**, 054311 (2023).
- [67] A. J. Gabourie, Z. Fan, T. Ala-Nissila, and E. Pop, Spectral decomposition of thermal conductivity: Comparing velocity decomposition methods in homogeneous molecular dynamics simulations, *Phys. Rev. B* **103**, 205421 (2021).
- [68] F. Knoop, T. A. R. Purcell, M. Scheffler, and C. Carbogno, Anharmonicity in thermal insulators: An analysis from first principles, *Phys. Rev. Lett.* **130**, 236301 (2023).
- [69] N. Ouyang, Z. Zeng, C. Wang, Q. Wang, and Y. Chen, Role of high-order lattice anharmonicity in the phonon thermal transport of silver halide  $AgX$  ( $X = Cl, Br, I$ ), *Phys. Rev. B* **108**, 174302 (2023).
- [70] Đ. Dangić, O. Hellman, S. Fahy, and I. Savić, The origin of the lattice thermal conductivity enhancement at the ferroelectric phase transition in GeTe, *npj Comput. Mater.* **7**, 57 (2021).
- [71] X. Li, K. Maute, M. L. Dunn, and R. Yang, Strain effects on the thermal conductivity of nanostructures, *Phys. Rev. B* **81**, 245318 (2010).
- [72] K. D. Parrish, A. Jain, J. M. Larkin, W. A. Saidi, and A. J. H. McGaughey, Origins of thermal conductivity changes in strained crystals, *Phys. Rev. B* **90**, 235201 (2014).
- [73] X. Meng, T. Pandey, J. Jeong, S. Fu, J. Yang, K. Chen, A. Singh, F. He, X. Xu, J. Zhou, W.-P. Hsieh, A. K. Singh, J.-F. Lin, and Y. Wang, Thermal conductivity enhancement in  $MoS_2$  under extreme strain, *Phys. Rev. Lett.* **122**, 155901 (2019).
- [74] Z. Zeng, S. Li, T. Tadano, and Y. Chen, Anharmonic lattice dynamics and thermal transport of monolayer InSe under equibiaxial tensile strains, *J. Phys.: Condens. Matter* **32**, 475702 (2020).